sciendo

Polish Journal of Chemical Technology, 26, 2, 31—41, 10.2478/pjct-2024-0015

Numerical Modeling of Heat Transfer and Flow Field in a Novel Calcinator

Tie-zhuang Zhou[1, 2], Bin Yang[1*], Cheng-qiang Wang[3]

[1]College of New Energy, China University of Petroleum Huadong (East China), Qingdao, China
[2]National Research Center for Drying Technology and Equipment Engineering Technology, Tianhua Chemical Machinery and Automation Institute Co., Ltd., Lanzhou, China
[3]Sinopec Research Institute of Petroleum Processing, Beijing, China
[*]*Corresponding author: e-mail:* b20150016@s.upc.edu.cn

This study focused on investigating the heat transfer and flow dynamics of a catalyst granule within a pilot calciner, employing both numerical modeling and computational fluid dynamics. The research comprised two primary components: (1) Simulation of the gas flow within the pilot calciner using the Eulerian–Eulerian approach, treating gases and catalyst particles as distinct phases – gas and granular. The model, encapsulating both heat transfer and flow processes, was developed in Fluent software version 16.0. Its accuracy was confirmed against empirical data from a pilot-scale calciner unit. (2) Subsequent to validation, the model was utilized to examine the distribution characteristics within the flow field, including the temperature profiles of gas and particles, the vector velocity field of the gas across different phases, and the overall heat transfer coefficient. This investigation aims to enhance the understanding of the complex heat transfer and flow dynamics in calciners, facilitating the optimization of operational parameters, performance, and structure of pilot-scale equipment. Furthermore, it provides foundational data pertinent to the future exploration of real-world industrial applications.

Keywords: Novel Calciner; Heat transfer; Flow field; Numerical modeling.

INTRODUCTION

Zeolites have found extensive use in the oil refining process as catalysts. Feedstock roasting constitutes a pivotal procedure in catalyst production. During this process, aluminum is extracted from the framework, leading to an elevation in the silica-to-alumina ratio and the acid site activity within the zeolite structure. These alterations in zeolite composition and characteristics exert a substantial influence on the catalytic stability, selectivity, activity, and octane rating of FCC gasoline[1, 2, 3]. The principle of dealumination in the calcination process is articulated as follows:

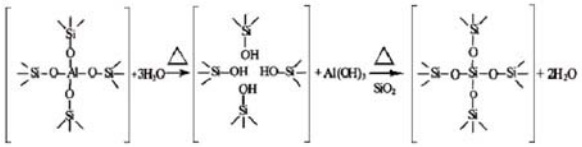

(1)

The performance of the calciner significantly affects the strength, activity, and quality of catalysts, as well as the overall energy consumption of the system. The primary physicochemical processes occurring in the calciner involve heat and mass transfer between particles and surfaces, as well as among particles themselves. As depicted in Figs. 1(a) and 1(b), both the heat transfer and the flow field within the calciner play pivotal roles in determining the characteristics of catalyst production. Optimal calcination conditions promote the formation of catalysts with high activity and stability. Numerical modeling of the calciner using computational fluid dynamics (CFD) tools can contribute to identifying optimal operational conditions and calcination structure designs that facilitate the production of highly active and stable catalysts. However, prolonged residence times may lead to structural defects and energy wastage . A more comprehensive scientific comprehension of the heat transfer and flow field within the calciner will yield deeper insights into the calcination processes, specifically in terms of

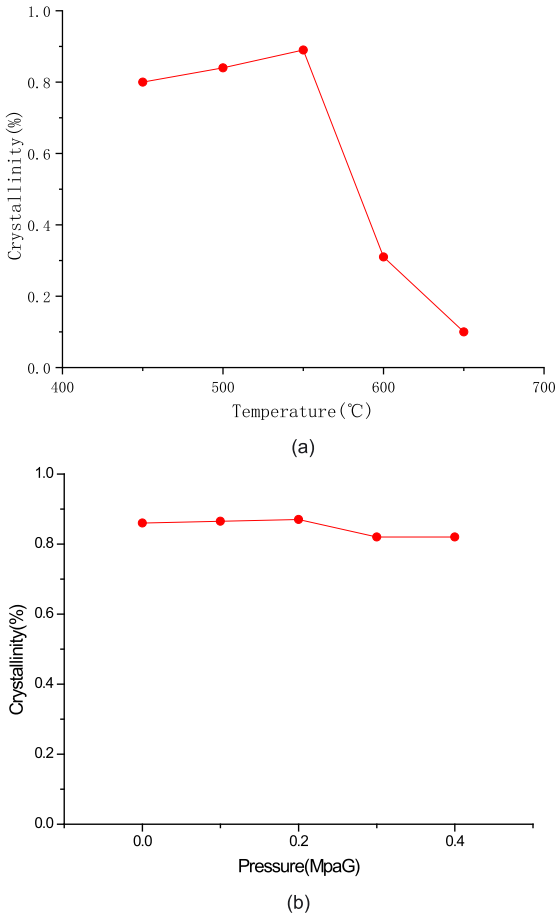

Figure 1. Variation in crystallinity with calcination temperature and pressure

how particles exchange heat with the heated plate and the high-temperature freeboard gas.

Numerical models employing CFD methods have been documented and explored within the domain of industrial roasting. Several factors, including velocity[5], gas-particle flow, heat transfer[6], particle retention time[7], and solid temperature[8] within the flow field, exert influence on catalyst activity by modifying the zeolite acid sites during

the roasting process. Marsh[9] conducted simulations of the complex behavior of a calciner furnace, considering the interplay of physical processes within a developed model. This approach significantly advances the design process by furnishing insights into particle composition and calcination rates within the calciner. Kanellis et al.[10] incorporated relevant heat transfer mechanisms, including both convection and radiation, to investigate a calcium looping pilot plant indirectly heated. The simulation results indicated that the model can provide an accurate prediction of realistic representations and pressure distribution characteristics when compared with data obtained from the pilot device. Chilka et al.[11] formulated a comprehensive CFD model, consolidating single and multiple particle experimental results, to simulate the distribution of temperature, flow field, and gas moisture content. These simulations effectively capture the influence of air flow patterns, air humidity, and temperature, demonstrating reasonable concurrence with measurement data. Zeneli et al.[12, 13] employed a three-dimensional CFD model to simulate the distribution of the flow field within the pilot calciner. The results, including pressure and temperature distribution, were assessed against experimental data along the calciner. Nakhaei et al.[14] utilized the multiphase particle-in-cell method in conjunction with the Eulerian-Lagrangian approach to investigate the heat transfer and dispersion of cold cement raw meal particles in a pilot-scale cement calciner. The results indicate that the model is capable of capturing gas-solid interactions and particle dispersion within the pilot-scale calciner. Xiao et al.[15] established a mathematical model to elucidate the calcining process of petroleum coke in a pot calciner, which was subsequently validated using industrial production data. This model has been employed to scrutinize the temperature field's distribution features and the vector velocity field of gas and solid phases. Kinekar et al.[16] improved operating conditions to reduce NO_X emissions by analyzing various characteristics of raw material and air stages. Zhu et al.[17] compared numerical simulations of pulverized coal with measured data, achieving good agreement in predicted parameters such as average temperature, decomposition rate, and NOx concentration compared to experimental data.

Of particular note, the efficiency of the calcination process is highly contingent on the aerodynamics of gas and solid phase motion within the calciner. Previous studies have predominantly focused on fluid dynamics in the calciner, with limited analysis of heat transfer efficiency and fluid characteristics during calcination. The utilization of CFD and numerical methods offers a deeper understanding and information that can facilitate design modifications to ensure superior calcination performance and product quality across varying production scales. Hence, it becomes crucial to develop appropriate physical and mathematical models to investigate flow and heat transfer, further enhancing calcination efficiency.

THE PRINCIPLE OF DEVICE AND DETERMINATION OF BOUNDARY CONDITIONS

Test Equipment and Operating Principle

As illustrated in Fig. 2(a), a calciner system comprises a feed tank, a rotary supply valve, a heating tube, a ther-

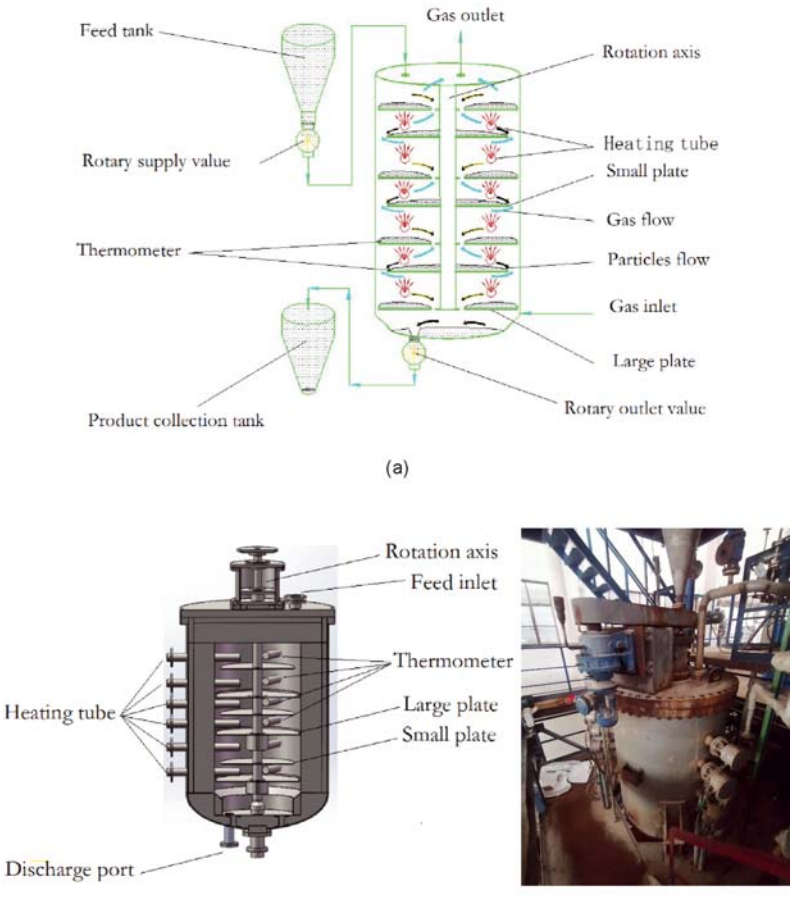

Figure 2. Working principles (a) and structure diagram (b) of the calciner

mometer, a large plate, a small plate, and a product collection tank. The three-dimensional configuration of the calciner is presented in Fig. 2(b).

The experiments were carried out in an industrial pilot plant vertical calciner with a geometry closely resembling that investigated in the simulations under atmospheric pressure and temperature conditions. This calciner possesses dimensions of 2.1 m in length and 1.1 m in internal diameter. Within the calciner, a configuration consisting of three small plates with external baffles and four large plates with internal baffles was installed in alternating sequences. Fig. 2 illustrates the operational principle of this innovative calciner.

The treated catalyst was introduced into the top of the calciner and descended to the first large plate. Both the rotating plate and baffles were securely affixed to the shell housing, facilitating the conveyance of the product in a spiral pattern across the heated plates toward the inner rim. Subsequently, the product descended from the inner hole to the lower-positioned small plate, where it was directed toward the outer edge. It then descended further to the lower large plate, where continuous rotary motion of the plate guided it toward the inner edge. This flow pattern was reiterated along the vertical extent of the calciner until the product exited from the bottom. A rotary valve was employed to introduce the catalyst into the calciner at a consistent rate. Notably, the direction of gas flow within the calciner was opposite to that of particle flow, thereby facilitating enhanced mass and heat transfer in this counterflow process.

To investigate heat transfer and flow dynamics within the calciner, FLUENT 16.0 software and a numerical model were utilized to simulate the calcination process. The Eulerian-Eulerian model was chosen due to the low Reynolds numbers near the wall. The gas inlet was specified with a temperature of 138 °C and a velocity of 7 m/s. The gas outlet pressure was set at 4 bar, with the turbulence intensity and hydraulic diameter specified accordingly in the model. A linear rotation speed of 20 rad/min was defined. The simulation boundary conditions are detailed in Table 1. The material particle flow at the inlet was set at 0.0056 kg/s with an inlet temperature of 25 °C. The properties of the particles and inlet gas are presented in Table 2.

Mathematical Model

Turbulence Models

The process of catalyst roasting involves a complex interplay of gas-solid two-phase mass and heat transfer, chemical reactions, particle mixing, and fluidization within the calciner. The mechanisms governing the processes within the rotary calciner are primarily influenced by turbulence. Therefore, in previous research[18, 19], a simplified simulation model predicting heat transfer and flow field mechanisms based on a standard k-ε turbulence model was proposed.

This simulation and numerical model are constructed on the following assumptions: (1) The catalyst is treated as a fluid with identical heat transfer characteristics to solids, and (2) the article neglects the processes of moisture evaporation and chemical reactions. Respectively, Eq. (2) represents the gas continuity equation, while Eq. (3) through (5) pertain to the gas phase momentum conservation equation. Eqs (6) and (7) correspond to the standard k-ε turbulence model, and Eq. (8) deals with turbulent stresses.

$$\frac{\partial \rho}{\partial t}+\frac{\partial(\rho \mathrm{u})}{\partial x}+\frac{\partial(\rho v)}{\partial y}+\frac{\partial(\rho w)}{\partial z}=0 \tag{2}$$

In Eq. (2), is the velocity of the gaseous phase (m/s), and is the density of the continuous phase gas.

$$\frac{\partial(\rho u)}{\partial t}+\operatorname{div}(\rho u \mathrm{u})=-\frac{\partial(\mathrm{p})}{\partial x}+\frac{\partial\left(\tau_{xx}\right)}{\partial x}+\frac{\partial\left(\tau_{yx}\right)}{\partial y}+\frac{\partial\left(\tau_{zx}\right)}{\partial z}+F_x \tag{3}$$

$$\frac{\partial(\rho v)}{\partial t}+\operatorname{div}(\rho v \mathrm{u})=-\frac{\partial(\mathrm{p})}{\partial y}+\frac{\partial\left(\tau_{xy}\right)}{\partial x}+\frac{\partial\left(\tau_{yy}\right)}{\partial y}+\frac{\partial\left(\tau_{zy}\right)}{\partial z}+F_y \tag{4}$$

$$\frac{\partial(\rho w)}{\partial t}+\operatorname{div}(\rho w \mathrm{u})=-\frac{\partial(\mathrm{p})}{\partial z}+\frac{\partial\left(\tau_{xz}\right)}{\partial x}+\frac{\partial\left(\tau_{yz}\right)}{\partial y}+\frac{\partial\left(\tau_{zz}\right)}{\partial z}+F_z \tag{5}$$

$$\frac{\partial(\rho \kappa u_i)}{\partial t}=\frac{\partial(p)}{\partial \mathrm{x}_i}\left[\left(\mu+\frac{\mu_t}{\sigma_s}\right)\frac{\partial k}{\partial x_j}\right]+G_k+G_b-\rho\varepsilon-Y_M \tag{6}$$

$$\frac{\partial(\rho \kappa u_i)}{\partial t}=\frac{\partial(p)}{\partial \mathrm{x}_i}\left[\left(\mu+\frac{\mu_t}{\sigma_s}\right)\frac{\partial k}{\partial x_j}\right]+\frac{C_1 C_k \varepsilon}{k}-\frac{C_2 \rho \varepsilon^2}{k} \tag{7}$$

$$\tau_{ij}=2\left(\left(\mu+\mu_t\right)/\mathrm{Re}_\infty\right)\left(S_{ij}-\frac{S_{\mathrm{nn}}\delta_{xy}}{3}\right)-2\rho k\delta_{ij}/3 \tag{8}$$

In Eqs. (2)~(7), τ_{xy}, τ_{xz}, τ_{yz} is the viscous stress component in the continuous phase, F_x, F_y, F_z is the F component in the X, Y and Z directions, P is the static pressure, G_K is the turbulent kinetic energy caused by an average velocity gradient, G_b is the turbulent kinetic energy caused by buoyancy, ε is the dissipation rate, and Y_M is the influence of pulsation expansion on the total dissipation rate in compressible turbulence.

Energy Transfer Models

Energy conservation equation:

$$\frac{\partial\left(\rho T_i\right)}{\partial t}+div(\rho \mathrm{uT})=div\left(\frac{k}{C_p}gradT\right)+S_T \tag{9}$$

In Eq (8), k is the thermal conductivity (w/°C·m), T is the gas temperature (°C), c_p is the enthalpy (J/kg), and S_T is the volumetric heat source (kg/s^3·m).

The heat transfer process in the baking furnace can be summarized as follows: Following the reception of

Table 1. Boundary type and simulation conditions

Boundary	Types	Value range
Gas-flow inlet	Speed inlet	7 m/s
Gas-flow outlet	Pressure outlet	40000 Pa
Gas-inlet temperature	/	138 °C
Rotational plate	Rotary sidewall	20 rad/min

Table 2. The properties of particles and inlet gas

Materials	Density/ (kg/m^3)	Viscosity coefficient / (10^{-5} Pa·s)	Thermal Conductivity /(W/(°C·m))	Specific heat at constant Pressure/(KJ/(kg·°C))
Particles	780	/	0.252	1.17
Gas	2.16	1.39	0.028	2.29

external heat source energy by the surface of the heating tubes, a portion of this energy is transferred to the rotating plate and the injected gas during the roasting process. Subsequently, the particles undergo simultaneous heating from both the high-temperature plate and fluid convection. Consequently, heat transport within the vertical calciner occurs through several mechanisms, including radiation heat transfer between the heating tubes and the rotation plate, convective and radiation heat transfer between the heating tubes and the gas, convective heat transfer between particles and fluid convection, thermal conduction between the plate and the particles, thermal conduction within the particles, and thermal conduction and radiation heat transfer between the surfaces of the particles. The mechanism of the heat transfer process within the calciner is illustrated in Fig. 3. This study primarily focuses on the mechanisms of thermal and fluid convection conduction, which are expected to predominate when the radiation tube temperature is low and when it is not in direct contact with the particles.

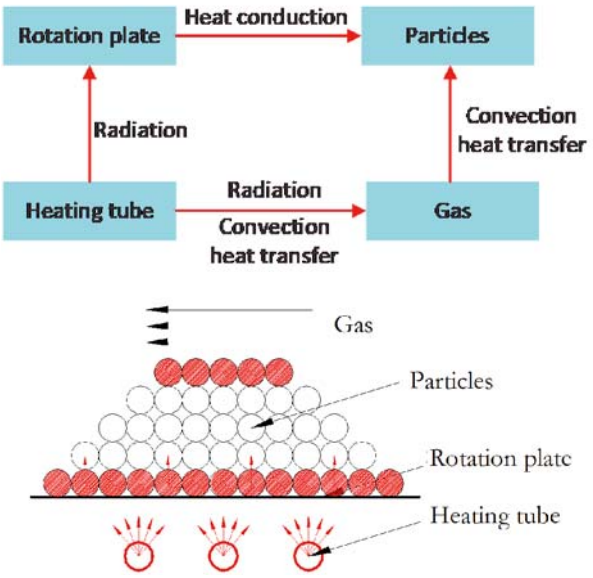

Figure 3. Heat transfer mechanism of particles in the calciner

The mechanism of heat transfer diffusion within the plate is depicted in Fig. 4. The temperature gradient within the calciner propels heat from the high-temperature region to the low-temperature region. Concurrently, the regular stirring of particles by the baffle, facilitated by the rotation of the plate, leads to a randomized distribution of particles with varying temperature levels. This, in turn, enhances the heat transfer process and contributes to greater uniformity in the temperature of the material layers[20, 21].

The heat transfer coefficient between the rotating heating plate and the catalyst particles is calculated as follows:

$$h_p = \frac{4\lambda_g}{d_p}\left[\left(1+\frac{2\sigma}{d_p}\right)\ln\left(1+\frac{d_p}{2\sigma}\right)-1\right] \tag{10}$$

where h_p is the theoretical contact heat transfer coefficient (W/m$^2\cdot$ °C) between the rotating plate and granular material, h_s is the theoretical contact heat transfer coefficient (W/m$^2\cdot$ °C) that considers the surface covering coefficient, d_p is the diameter of granular material (m), λ_p is the thermal conductivity (W/m$^2\cdot$ °C) of air between particles, C_p is the specific heat of intergranular gas (J/m$^2\cdot$ °C), M is the molecular weight of gas kg/(kmol), is the roasting temperature (°C), and ψ is the surface covering factor of the rotating plate.

The coefficients of and are given by the following expression:

$$\sigma = \frac{2(2\text{-}\gamma)}{\gamma}\sqrt{\frac{2\pi RT}{M}}\frac{\lambda_g}{p\left(2C_g - R/M\right)} \tag{11}$$

$$h_s = \Psi h_p \tag{12}$$

The heat transfer coefficient considering the effect of air is given by:

$$\lg\left(1/\gamma - 1\right) = 0.6 - \left(1000/T + 1\right)/2.8 \tag{13}$$

In the completely mixed state, the heat conduction coefficient of particles was defined as follows:

$$h_c = \sqrt{\frac{\lambda_p C_p \rho}{\pi\tau_R}} \tag{14}$$

where h_c is the heat conduction coefficient of particles (W/m$^2\cdot$ °C), C_p is the specific heat of particles (J/m$^2\cdot$ °C), ρ is the density of particles (kg/m^3), and λ_e is the thermal conductivity (W/m$^2\cdot$ °C) of particles.

When considering the fixed particle layer shown in Fig. 5, the heat transfer coefficient between the particles and the rotating plate was expressed as follows:

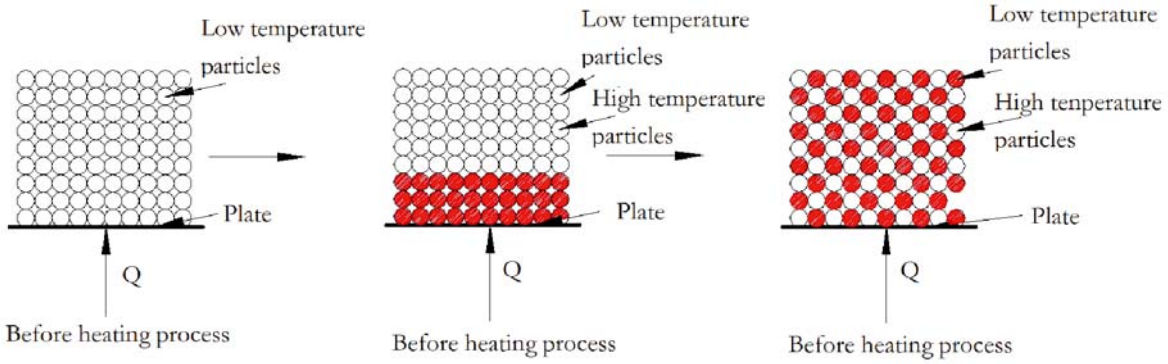

Figure 4. The diffusion heat transfer mechanism of particles in the plate

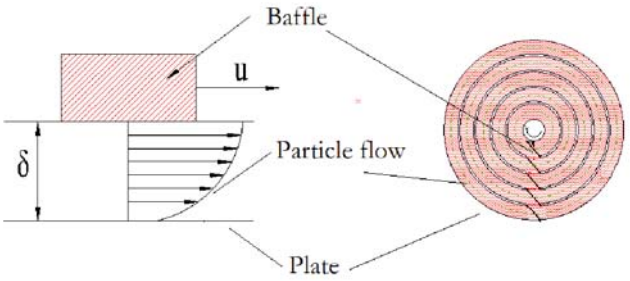

Figure 5. Schematic diagram of the heat transfer of particles in the plate

$$h_i = \frac{1}{\frac{1}{h_s}+\frac{1}{h_c}+\frac{1}{h_{hs}}+\frac{\delta}{\lambda_e}} \tag{15}$$

where h_{hs} is the free convection heat transfer coefficient of the gas.

Because the heat transfer coefficient h_{hs} was much greater than h_s and h_c, the simplified expression of Eq. (15) was defined as follows:

$$h_i = \frac{1}{\frac{1}{h_s}+\frac{1}{h_c}+\frac{\delta}{\lambda_e}} \tag{16}$$

Finally, by applying Eqs. (12), (14) and (16), the heat transfer coefficient is written in Eq. (17):

$$h = \frac{1}{\tau}\int_0^{\tau} h_i d\tau$$

$$= \frac{2h_s\lambda_e\left(\lambda_e+\delta h_s\right)^2 C_p\rho_b}{\left(\lambda_e+\delta h_s\right)\tau\pi\lambda_e h_s^2}\left[\sqrt{\frac{\tau\pi\lambda_e h_s^2}{\left(\lambda_e+\delta h_s\right)^2 C_p\rho_b}} - \right. \tag{17}$$

$$\left. -\ln\left(1+\sqrt{\frac{\tau\pi\lambda_e h_s^2}{\left(\lambda_e+\delta h_s\right)^2 C\rho_b}}\right)\right]$$

Dimensionless analysis of the convective coefficient:

The factors that affect the free convective coefficient h' include the characteristic size of the viscosity (μ), gas density (ρ), rotating plate (D), specific heat capacity (C_p), thermal conductivity (λ) and buoyancy ($\Delta\rho g$) of the fluid per unit volume. The free convective coefficient of the gas can be expressed as

$$h' = f\left(D,\rho,\mu,c_p,\lambda,\Delta\rho g\right) \tag{18}$$

The 3 random variables based on 4 basic dimensions, length (D), mass (M), time (τ) and temperature (T), are contained in Eq. (18). The dimensions of the physical quantity are shown in Table 3.

When adopting the dimensionless parameter method, the equation above becomes

$$\pi_1 = \phi\left(\pi_2,\pi_3\right) \tag{19}$$

where π_1, π_2 and π_3 is expressed as

$$\begin{cases} \pi_1 = \mathrm{D}^a\lambda^b\mu^c\left(\rho g\beta\Delta t\right)^d h' \\ \pi_2 = \mathrm{D}^e\lambda^f\mu^g\left(\rho g\beta\Delta t\right)^i\rho \\ \pi_3 = \mathrm{D}^j\lambda^k\mu^m\left(\rho g\beta\Delta t\right)^n c_p \end{cases} \tag{20}$$

The dimensions in Table 3 were substituted into Eq. (20), the equation above becomes

$$\begin{cases} \pi_1 = \dfrac{\mathrm{D}h'}{\lambda} = Nu \\ \pi_2 = \dfrac{c_p\mu}{\lambda} = \mathrm{Pr} \\ \pi_3 = \dfrac{\mathrm{D}^3\rho^2 g\beta\Delta T}{\mu^2} = Gr \end{cases} \tag{21}$$

The dimensionless parameter free convective coefficient h' was expressed as follows:

$$h' = c\left(Gr\right)^a\left(\mathrm{Pr}\right)^b = c\left(\frac{\mathrm{D}^3\rho^2 g\beta\Delta T}{\mu^2}\right)^a\left(\frac{c_p\mu}{\lambda}\right)^b\left(\frac{\lambda}{D}\right) \tag{22}$$

Particle temperature model:

As illustrated in Fig. 2, the particles on the rotating plate are primarily heated through the heat conduction of the rotating plate and convective heat transfer from the flowing hydrothermal fluid. Consequently, applying the principle of heat conservation, wherein heat input minus heat output equals heat accumulation, the total energy (Q) absorbed by the particles can be expressed as:

$$h_s = \Psi h_p \tag{23}$$

$$Q = q_m C_p\left(t_2-t_1\right) = \left(hS\Delta t_m + h'S\Delta t_m\right)\tau = \left(h+h'\right)\tau S\Delta t_m \tag{24}$$

In Eq. (24), and are given by

$$\Delta t_m = \frac{t_2-t_1}{\ln\dfrac{T-t_1}{T-t_2}} \tag{25}$$

$$q_m = \rho SL \tag{26}$$

where Δt_m and q_m can be obtained from Eqs. (25) and (26), respectively, the temperature of particles t_2 can be written as Eq. (28):

$$t_2 = T - \frac{T-t_1}{e^{\frac{(h+h')\tau}{\rho LC_p}}} \tag{28}$$

where the temperature of plate T was 500 °C, the thermodynamic constant R was 8.314 J(mol · °C), the molar mass of gas M was 18, the thermal conductivity of the gas inner-granular λg was 0.0574 W(mol · °C), the particle size was 0.001 m, the surface coverage rate was 0.95, and the thermal conductivity of the particles λp was 1.3 W(mol · °C). The specific heat capacity Cp of the particles is 1250 J(mol · °C), the density ϱ of the particles is 780 kg/m^3, and the free convective coefficient h' is 60 W(mol · °C).

Table 3. Geometrical parameters of agitated vessel

	Free convective coefficient	Character-istic size	Density	Viscosity	Specific heat capacity	Thermal conductivity	Buoyancy
Symbol	h'	D	ρ	μ	c_p	λ	$\Delta\rho g$
Dimension	$M\tau^{-3}T^{-1}$	L	ML^{-3}	$ML^{-1}\tau^{-1}$	$L^2\tau^{-2}T^{-1}$	$ML\tau^{-3}T^{-1}$	$L\tau^{-1}$

Experimental method of mean residence time

In this study, experiments were conducted in an industrial pilot plant calciner with a geometry closely resembling that examined in the simulations under atmospheric pressure and temperature conditions. The experimental measurements of tracers and mean residence time (MRT) within the calciner are depicted in Fig. 6. Bluish tracers, bearing a close resemblance to the original catalysts, were introduced in this experiment. Once a steady state was reached, the tracers were sequentially introduced at the calciner inlet and collected at the calciner outlet after specific time intervals. Concurrently, the residence time of the tracers was rigorously recorded. The MRT of the tracers is expressed as:

$$\tau = \int_0^\infty \mathrm{t} \cdot E(t) \cdot d(t) \tag{29}$$

The can be mathematically expressed as

$$E(\mathrm{t}) = \frac{C(\mathrm{t})}{\int_0^\infty C(\mathrm{t}) \cdot d(t)} \tag{30}$$

Figure 6. The tracers and experimental images of MRT

Grid Generation

Utilizing the structural parameters outlined in Table 4, the geometric model (depicted in Fig. 7(a)) created in SolidWorks 2016 is imported into Fluent 16.0 software (as seen in Fig. 7(b)). For meshing the plate and particles, a structured tetrahedral mesh is employed, while a high-quality hexahedral mesh is applied in the fluid region. Ultimately, the fluid and solid regions are coupled together.

Table 4. Structural parameters of the model

Parameters	Size
length	2.1 m
width	1.1 m
Number of large plate	4
Number of small plate	3
Diameter of large plate	1.008 m
Diameter of small plate	0.85 m
Thickness of particles layer	0.027 m

Grid Independence Verification

To mitigate errors arising from grid resolution, the model's effectiveness was assessed by comparing results obtained from four different grid resolutions prior to initiating the simulation. As illustrated in Fig. 8(a), point A (450, 450, 1500) within the calciner was chosen for conducting a grid independence verification test. The simulated results are presented in Fig. 8(b), indicating minimal temperature variations when the grid count exceeded 3.12 million. Conversely, temperature fluctuations were more pronounced when the grid count fell below 3.12 million. In pursuit of enhanced computational efficiency, a grid resolution of 3.12 million was selected for the subsequent heat transfer and flow field simulation.

SIMULATION RESULTS AND DISCUSSION

The gas flow field within the pilot calciner was simulated using the Eulerian-Eulerian model, wherein gases and catalyst particles were treated as the gas

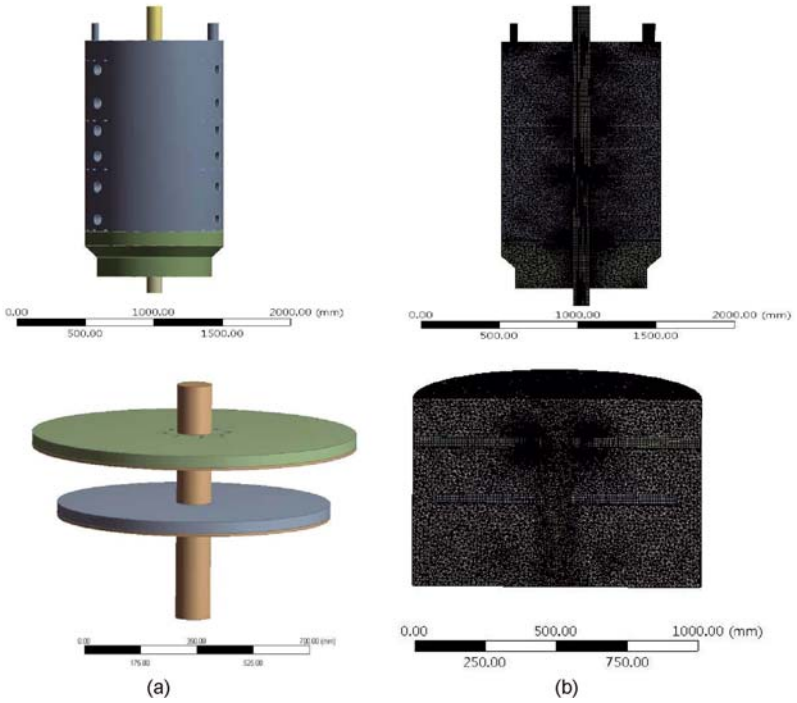

Figure 7. Grid division of the rotary calciner model

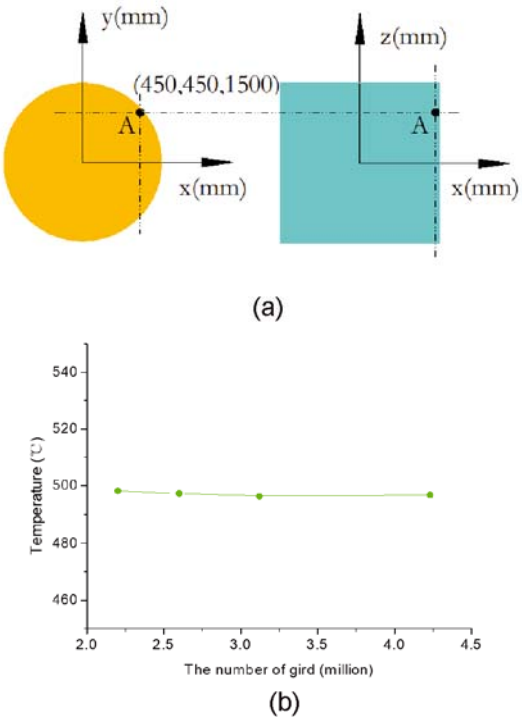

Figure 8. The model and results of grid independence verification

phase and granular continuous phase, respectively. The model for the heat transfer and flow field processes was implemented in Fluent software 16.0 and validated using a pilot-scale calciner unit. Following the validation analysis, the established model was employed to investigate the distribution characteristics of the flow field, the temperature field of gases and particles, the vector velocity field of gases among different phases, and the total heat transfer coefficient. The findings are summarized as follows:

Flow field

Figure 9 illustrates the velocity field within 8 layers of zones in the calciner. The gas flows exhibit a characteristic 'S' shape on the XZ plane, moving from the interior of the large plate to the exterior of the small plate and then back from the exterior of the small plate to the interior of the large plate. In theory, the axisymmetric structure should lead to a uniform velocity distribution within the calciner. However, due to the influence of the driving force exerted by the incoming gas, the gas velocity on the left is higher than that on the right in layers 1 and 2. In Fig. 10(a) and 10(b), the gas forms a low-speed flow area (0.2–0.8 m/s) in layer 1. Additionally, a circular flow zone (0.5–0.9 m/s) emerges on the left side of the velocity inlet, approximately 0~0.4 m from the rotation axis. This is attributed to the narrowing of the gas flow channel, leading to changes in the flow direction and pattern.

Within the central part of the large plate, the gas velocity rapidly increases after passing through the inner bore, resulting in the formation of a spraying-shaped flow zone (0.045–0.06 m/s) at the inlet of layer 2. Due to the alteration in gas flow direction, a substantial reflux zone characterized by a low-speed flow (0.7–1.5 m/s) manifests in the middle of layer 3, as shown in Fig. 10(c). In Fig. 10(d), a low-speed recirculation zone (0.4–0.6 m/s) emerges on the upper side of layer 4 due to changes in fluid migration channels and gas viscosity. Figs. 10(e) and 10(g) reveal low-speed areas within the turbulent flow field in layers 5 and 7, a phenomenon driven by gas volume expansion, which strongly promotes the mixing and heat exchange of granules. However, local high-velocity circulation flows increase the risk of material being carried away by the gas. Fig. 10(f) and 10(h) depict the velocity distribution of gas flow in layers 6 and 8. A pronounced spray phenomenon occurs on the upper side of the plate, leading to the dispersion of agglomerated particles, facilitating thorough mass and heat exchange, and enhancing the calcination process.

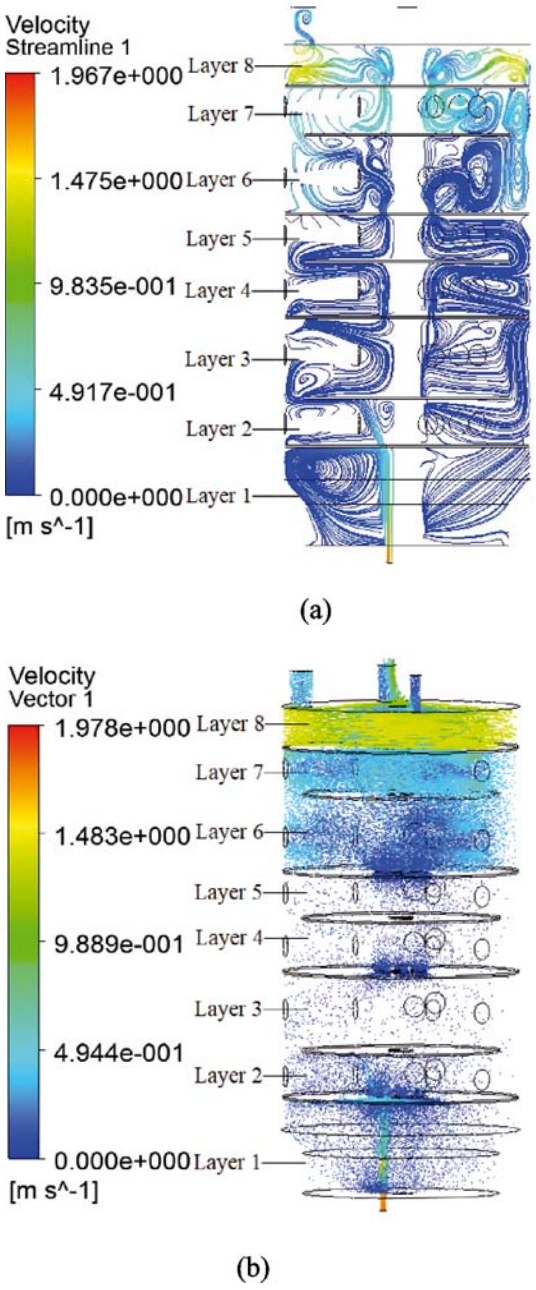

Figure 9. Velocity vectors of different zones on the XZ plane of the calciner

Total heat transfer coefficient

Fig. 11 illustrates the contour of the total heat transfer coefficient alongside the rotation angular velocity of the plate. It can be deduced that the total heat transfer co-

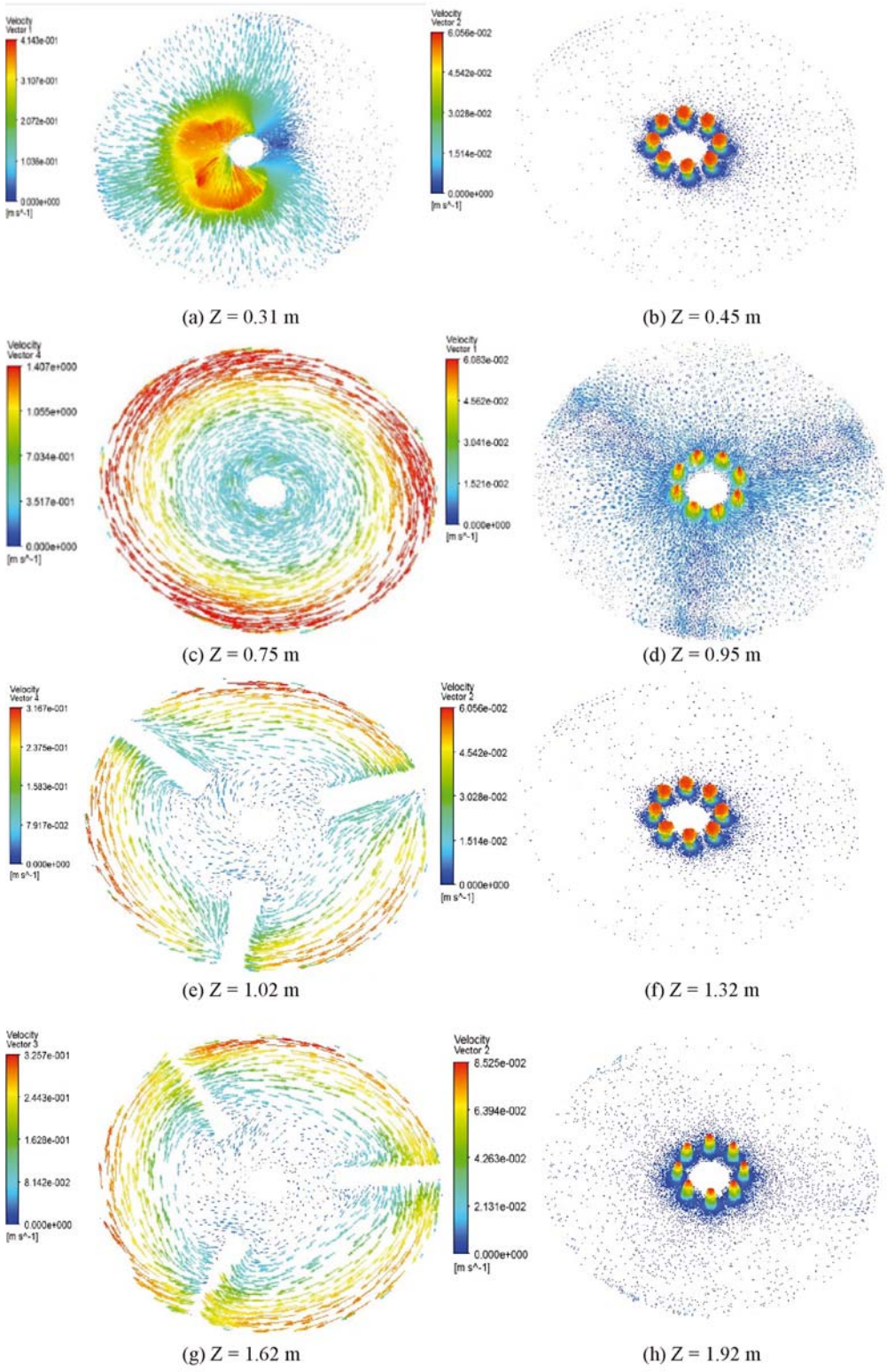

Figure 10. Velocity vectors of different zones on the XY plane of the calciner

efficient follows an expected increase with the rotation angular velocity of the plate. As the rotational angular velocity escalates from 20 rad/min to 170 rad/min, the particle mixing speed progressively accelerates, resulting in a rapid increase in the total heat transfer coefficient. Initially, heat conduction within the particles dominates this process. However, as the rotational angular velocity advances from 170 rad/min to 180 rad/min, the total heat transfer coefficient experiences a gradual increase, primarily driven by convective heat transfer from the gas.

Five different heat capacity values for the solid material were considered: 0.75, 1.0, 1.25, 1.5, and 1.75 kJ(kg · °C). As anticipated, particles with higher heat capacity exhibit a greater total heat transfer coefficient, which enhances heat transfer between particles.

Calcination conditions play a pivotal role in the catalyst production process. Optimizing the rotational angular speed can enhance heat transfer and facilitate the production of catalysts with high activity and stability. However, excessively high rotational speeds may lead to

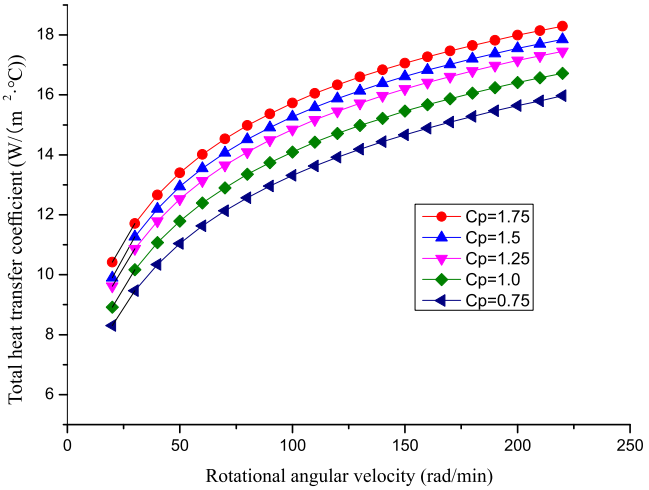

Figure 11. Simulated results under different angular rotations of the total heat transfer coefficient

a reduction in residence time and catalyst activity during the calcination process.

Temperature distribution

Figs. 12(a) and 12(b) depict the temperature field distributions within sections of layer 8 and layer 7 in the calciner, respectively. It is evident that the temperature distribution is generally uniform in the XZ plane, except for layer 1. The highest temperature within the calciner is located at the inner edge of Figs. 12(a) and the outer edge of Figs. 12(b), while lower-temperature regions are observed in the inlet section. This lower-temperature area corresponds to a substantial region where low-temperature particles absorb heat and undergo calcination reactions.

In Figs. 12(a), the temperature is lower at the plate's edge but gradually increases toward the center of the plate. A higher convective heat transfer coefficient promotes heat transfer among particles and enhances temperature uniformity within the calciner. Seven values of the convective heat transfer coefficient were considered: 10, 20, 30, 40, 50, 60, and 70 W(m^2 · °C). All simulations were conducted under a rotational speed of 20 rad/min. The evolution of temperature as a function of the convective heat transfer coefficient is presented in Fig. 12(c). As most particles attain higher temperatures, greater temperature uniformity is achieved in Figs. 12(b). Upon contact with the rotating disk, particles are rapidly heated by the flow of hot gas and the plate, resulting in a temperature of 261 °C within 5 min of residence time. This rapid heating is primarily due to the dominance of convective heat transfer at the feeding port, owing to the higher gas velocity.

In Figs. 12(a), the particle temperatures can reach 470.5 °C. As seen in Fig. 12(a) and 12(d), there is a significant increase in the particle temperature in the region located at the outlet of the first plate, particularly in the x-450 to x-500 plane. This increase is attributed to the movement of particles inward and downward, enhancing heat transfer between the particles and the gas phase. This results in a higher convective heat transfer coefficient for the particles to transfer heat with the hot gas.

Temperature distributions within the calciner are largely influenced by the temperature difference between the surrounding gas and the particle temperature. In the lower plate (Figs. 12(b)), as particles move outward on the small plate, the gas temperature curve becomes more uniform, leading to a slight increase in temperature. Ultimately, the temperature of the particles reaches 497 °C in Figs. 12(b), meeting the temperature requirements for the calcination process.

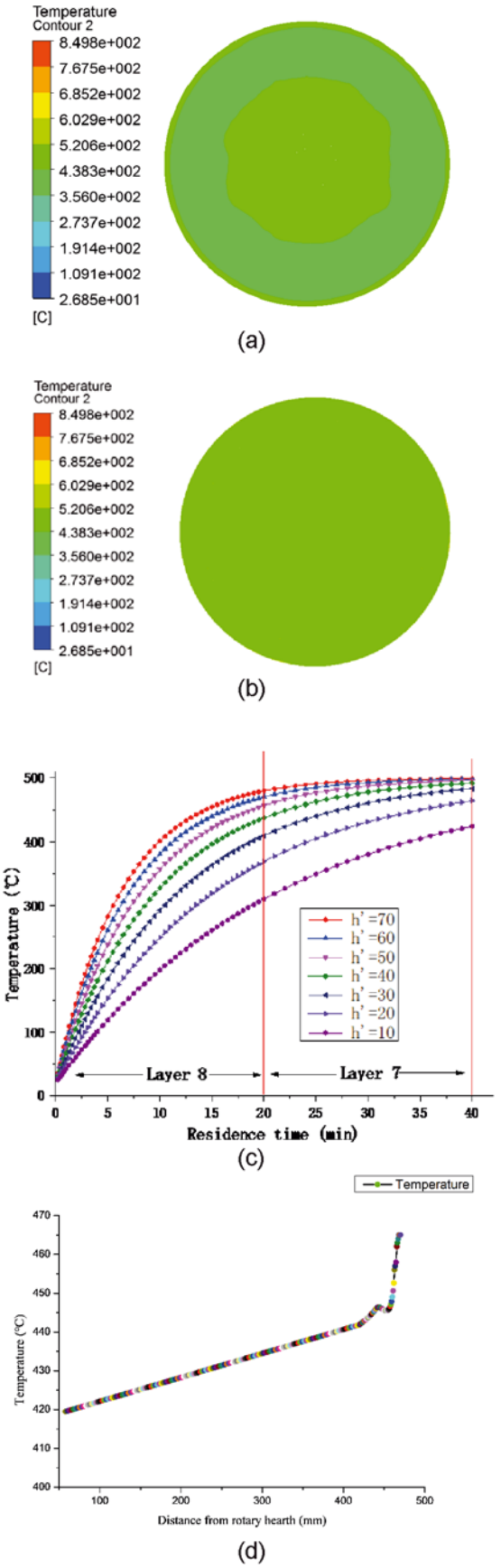

Figure 12. Simulated results of the temperature distributions in the calciner

Fig. 12(d) displays the temperature field distribution across different layers along the height of the calciner. It is evident that in layer 1, as one ascends the calciner, the gas temperature gradually increases from approximately 30 °C to 63 °C at the bottom of the calciner. This temperature rise is attributed to the sole heat transfer mode being between the plate and gas. As low-temperature gas enters layer 2, its temperature undergoes a rapid increase due to heat supplied from the radiation tube in layer 2. In this region, the maximum temperature can reach 510 °C.

Subsequently, the gas temperature decreases due to heat transfer to the raw material. After a series of alternating increases and decreases, the temperature eventually stabilizes at approximately 500 °C, indicating that a steady state is reached along the height of the calciner.

Comparison of simulations and experiments of temperature distribution

Temperature measurements within the calciner were conducted using four sensors positioned along the side of the calciner, as depicted in Fig. 13a. The comparison between the temperature distribution based on practical data from the four measurement points and the simulated temperature distribution along line 1 and line 2 is presented in Fig. 13b. In Fig. 13, lower-temperature gas enters the calciner under positive pressure, remains unheated by the thermal tube, and rapidly diffuses, resulting in a low-temperature region (130–150 °C) at the bottom zone.

As shown in Fig. 13a, high-temperature areas (715–889 °C) are formed on both sides of the thermal tube due to direct heating from the heating tube. Furthermore, relatively high-temperature calcining zones with leftward high and rightward low temperatures are established in the upper area, with temperatures ranging from approximately 550–600 °C (leftward area) and 500–550 °C (rightward area). These temperatures meet the basic requirements for catalyst calcination.

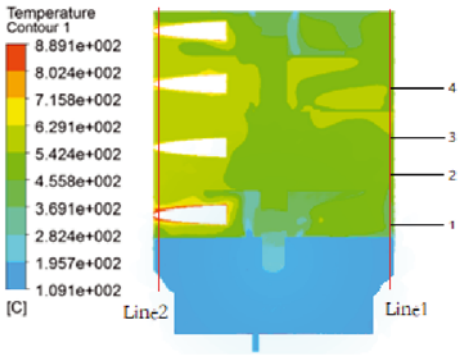

(a)

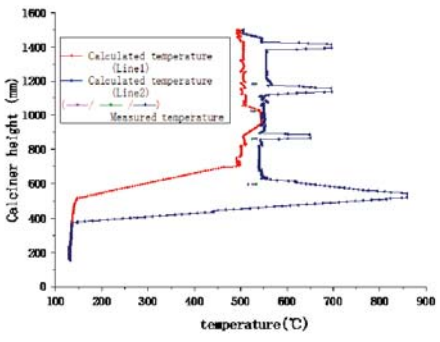

(b)

Figure 13. Temperature distribution on the center longitudinal cross section of the calciner

In Fig. 13b, the temperature along line 1 is higher than that along line 2. This discrepancy arises from the fact that the region surrounding the thermal tube is more easily heated than areas farther away. Therefore, the measurement and adjustment of gas temperature at suitable points are critical factors for a successful industrial calcination process. As evident in Fig. 13b, the calculation results based on the CFD model exhibit a consistent trend with the experimental data. The relative error falls within the range of 3.0% to 8.0%, confirming the fundamental temperature distribution within the calcination process

CONCLUSION

To analyze the heat transfer and flow field of catalyst granules in a pilot calciner using a numerical model and CFD method, the gas flow field of the pilot calciner was simulated utilizing the Eulerian–Eulerian model, treating gases and catalyst particles as gas and granular continuous phases. The model for the heat transfer and flow field process was implemented in Fluent software 16.0 and validated using a pilot-scale calciner unit. Following the validation analysis, the established model was applied to investigate the distribution features of the flow field, the temperature field of gas and particles, the vector velocity field of the gas among different phases, and the total heat transfer coefficient. The results are summarized as follows:

A low-speed turbulent flow field was observed in layers 5 and 7 due to the expansion of gas volume, enhancing the mixing and heat exchange of granules. However, local high-velocity circulation flow increases the risk of material being carried away by gas.

Significant temperature increases were observed in regions near the outlet of the first plate, where intense heat exchange occurred between particles and the gas phase. Material temperatures reached 490 °C.

The calculation of temperature exhibited an error of no more than 6.0% compared to the actual measurement data throughout the calculation process, indicating good agreement between the numerical results and measured results.

Furthermore, this research provides a theoretical foundation for a deeper understanding of the complex heat transfer and flow field processes within the novel calciner. It also aids in optimizing the working parameters, performance, and structure of pilot equipment while offering fundamental data for future studies in actual industrial applications.

ACKNOWLEDGMENTS

This research was supported by the National Key Research and Development Plan of China (No. 2022YFB3504000) and the Gansu Provincial Science and Technology Plan of the Major Project (No. 22ZD-6GA024). We are grateful to Dr. Chengqing Wang for the effective discussions on rotary kiln transport processes.

The contributions of Y. Q. and Y. B. Xie to this study are acknowledged gratefully.

LITERATURE CITED

1. Serrano, D.P., García, R.A., Linares, M. & Gil, B. (2012). Influence of the calcination treatment on the catalytic properties of hierarchical ZSM-5. *Chem. Eng. Sci*. 179(1), 91–101. DOI: 10.1016/j.cattod.2011.06.029.

2. Scherzer, J. (1990). Octane-enhancing, Zeolitic FCC Catalysts: Scientific and Technical Aspects. *Catal. Rev. Sci. Eng*. 31(3), 215–354. DOI: 10.1002/chin.199025325.

3. Kunkeler, P.J., van der Waal, J.C., van Bokhoven, J.A., Koningsberger, D.C. & van Bekkum, H. (1998). The Relationship Between Calcination Procedure, Aluminum Configuration and Lewis Acidity. *Chem. Eng. Sci*. 180(2), 234–244. DOI: 10.1006/ jcat.1998.2273.

4. Da Ros, S., Barbosa-Coutinho, E., Schwaab, M., Calsavara, V., Fernandes-Machado & Nádia R.C. (2013). Modeling the effects of calcination conditions on the physical and chemical properties of transition alumina catalysts. *Mater. Char.* 80, 50–61. DOI: 10.1016/j.matchar.2013.03.005.

5. Shahrbabaki, A.S., Kalantar, V. & Mansouri, S.H. (2023). Analytical and numerical considerations of the minimum fluidization velocity of the molybdenite particles. *Mater. Mater. Mech.* 10(4), 769–776. DOI: 10.1007/s40571-022-00528-z.

6. Yang, L. & Farouk, B. (1997). Modeling of solid particle flow and heat transfer in rotary kiln calciners. *J. Air & Waste Manage. Assn*. 47(11), 1189–1196. DOI: 10.1080/10473289.1997.10464069.

7. Mikulčić, H., von Berg, E., Vujanović, M., Priesching, P., Tatschl, R. & Duić, N. (2012). CFD analysis of a cement calciner for a cleaner cement production. *Chem. Eng. Trans*. 29, 1513–1518. DOI: 10.3303/CET1229253.

8. Johansson, S., Westerberg, L.G. & Lundstrom, T.S. (2014). Gas and particle flow in a spray roaster. *JAFM*, 7(2), 187–196. DOI: 10.36884/jafm.7.02.20339.

9. Marsh, C. (2009). CFD modelling of alumina calciner furnaces. In Seventh International Conference on CFD in the Minerals and Process Industries, Melbourne, 1-4.

10. Kanellis, G., Zeneli, M., Nikolopoulos, N., Hofmann, C., Ströhle, J., Karellas, S. & Konttinen, J. (2023). CFD modelling of an indirectly heated calciner reactor, utilized for CO_2 capture, in an Eulerian framework. *Fuel*, 346, 128251. DOI: 10.1016/j.fuel.2023.128251.

11. Chilka, A.G. & Ranade, V.V. (2019). CFD modelling of almond drying in a tray dryer. *Chem. Eng. Sci*. 97(2), 560–572. DOI: 10.1002/ cjce.23357.

12. Zeneli, M., Nikolopoulos, A., Nikolopoulos, N., Grammelis, P., Karellas, S. & Kakaras, E. (2017). Simulation of the reacting flow within a pilot scale calciner by means of a three phase TFM model. *Fuel Process. Technol*. 162, 105–125. DOI: 10.1016/j.fuproc. 2017.03.032.

13. Havryliv, R. & Maystruk, V. (2017). Development of combustion model in the industrial cyclone-calciner furnace using CFD-modeling. *Chem. Chem. Technol*. 11(1), 71–80. DOI: 10.23939/chcht11.01.071.

14. Nakhaei, M., Hessel, C.E., Wu, H., Grévain, D., Zakrzewski, S., Jensen, L.S., Glarborg P. & Dam-Johansen, K. (2018). Experimental and CPFD study of gas–solid flow in a cold pilot calciner. *Powder Technol*. 340, 99–115. DOI: 10.1016/j. powtec.2018.09. 008.

15. Xiao, J., Huang, J., Zhong, Q., Zhang, H. & Li, J. (2016). Modeling and simulation of petroleum coke calcination in pot calciner using two-fluid model. Jom, 68, 643–655. DOI: 10.1007/s11837-015-1667-2.

16. Kinekar, S., Mone, S., Taqi, A., Mane, P., Gawali, B. & Vitankar, V. (2021). NOX reduction in calciner using air staging and raw meal split technology. *Mat. Today*, 45, 3091–3096. DOI: 10.1016/j.matpr.2020.12.143.

17. Zhu, J. & Kao, H. (2021). Numerical Simulation of Co-Combustion of Pulverized Coal and Different Proportions of Refused Derived Fuel in TTF Precalciner. *JRM*. 9(7), 1329. DOI: 10.32604/jrm.2021.015079.

18. Xu, J. & Ma, Y. (2018). Simulation Analysis of Gas-solid Two-phase Flow for Heating Catalyst in Rotary Multi-cavity Kiln. ICMT., 398(1) 012010. DOI: 10.1088/1757-899X/398/1/012010.

19. Liu, X. & Jiang, J. (2004). Mass and heat transfer in a continuous plate dryer. Drying Technol. 22(7), 1621–1635. DOI: 10.1081/DRT-200025619.

20. Schlünder, E.U. (1988). On the mechanism of the constant drying rate period and its relevance to diffusion controlled catalytic gas phase reactions. *Chem. Eng. Sci*. 43(10), 2685–2688. DOI: 10.1016/0009-2509(88)80012-5.

21. Chaudhuri, B., Muzzio, F.J. & Tomassone, M.S. (2006). Modeling of heat transfer in granular flow in rotating vessels. *Chem. Eng. Sci*. 61(19), 6348–6360. DOI: 10.1016/j. ces.2006.05.034.